# Three-Dimensional Atomic-Scale Tomography of Buried Semiconductor Heterointerfaces

Koelling, Sebastian; Stehouwer, Lucas E.A.; Paquelet Wuetz, Brian; Scappucci, Giordano; Moutanabbir, Oussama

**DOI**
10.1002/admi.202201189

**Publication date**
2022

**Document Version**
Final published version

**Published in**
Advanced Materials Interfaces

ADVANCED MATERIALS INTERFACES
www.advmatinterfaces.de



# Three-Dimensional Atomic-Scale Tomography of Buried Semiconductor Heterointerfaces

*Sebastian Koelling,* Lucas E. A. Stehouwer, Brian Paquelet Wuetz, Giordano Scappucci, and Oussama Moutanabbir*

**Atom probes generate three-dimensional atomic-scale tomographies of material volumes corresponding to the size of modern-day solid-state devices. Here, the capabilities of atom probe tomography are evaluated to analyze buried interfaces in semiconductor heterostructures relevant for electronic and quantum devices. Employing brute-force search, the current dominant reconstruction protocol to generate tomographic three-dimensional images from Atom Probe data is advanced to its limits. Using Si/SiGe heterostructure for qubits as a model system, the authors show that it is possible to extract interface properties like roughness and width that agree with transmission electron microscopy observations on the sub-nanometer scale in an automated and highly reproducible manner. The demonstrated approach is a versatile method for atomic-scale characterization of buried interfaces in semiconductor heterostructures.**

## 1. Introduction

The properties of interfaces are known to have a significant influence on the performance of optical, electrical, and quantum devices.[1–5] In his Nobel acceptance speech 20 years ago, Herbert Kroemer famously noted, the interface is the device,[6] an insight that prevailed.[7]

Characterizing buried interfaces in heterostructures at the sub-nanometer scales relevant for the current generation of nanodevices is challenging. Widely used techniques for atomic-scale imaging like scanning probe microscopy and electron microscopy can typically not tackle this issue.[8–11] The former is restricted to the imaging of surfaces and the latter typically yields two-dimensional projections and hence does not resolve the third dimension of the interface.

Atom probe tomography (APT) with its capability of imaging the local chemistry in three-dimensions at the near atomic scale is a prime candidate for achieving atomic-scale characterization of buried interfaces.[12–15] However, limitations arising from the comparatively simple algorithms to reconstruct APT data are known to cause significant aberrations near interfaces, limiting accuracy.[12,16–18]

One way to address this issue is to improve APT data reconstruction using simulations or calibrations from electron tomography.[19,20] Both approaches are however time consuming and rely on information not readily available from an APT analysis.

Here, we propose an alternative approach. Instead of trying to correctly reconstruct the entire volume analyzed in the tomography, we develop a protocol that allows us to choose a set of reconstruction parameters for one interface at a time by combining brute force search with a simple, standard reconstruction algorithm[16] from data exclusively acquired during APT. We present a fully automated process that is highly reproducible and enables us to characterize interface widths and roughness on a sub-nanometer scale.

## 2. Buried Interfaces and the Hemispherical Constraint in APT Data Reconstruction

The issue typically faced during the analysis of buried interface in APT is highlighted in **Figure 1**.

Figure 1a shows a transmission electron microscopy (TEM) image of a strained silicon quantum well (QW) sandwiched between two $Si_{68}Ge_{32}$ layers. This heterostructure is developed for spin qubits in gate-defined quantum dots and nanosheet transistors.[3,21] For both technologies, sharp and reproducible interfaces are of utmost importance: in the quantum bit to achieve uniform valley splitting and hence to enable a scalable technology for quantum processors and in the transistors to allow for the controlled formation of nanosheets.[3,22]

The heterostructure for qubits can readily be analyzed using APT as shown in Figure 1b–e. Unfortunately, the standard data reconstruction method, which models the measurement as an azimuthal projection[23] from a hemisphere onto the

S. Koelling, O. Moutanabbir
Department of Engineering Physics
École Polytechnique de Montréal
Succursale Centre-Ville
Montréal H3C 3A7, Canada
E-mail: sebastian.koelling@polymtl.ca

L. E.A. Stehouwer, B. Paquelet Wuetz, G. Scappucci
QuTech and Kavli Institute of Nanoscience
Delft University of Technology
Delft 2600 GA, The Netherlands

The ORCID identification number(s) for the author(s) of this article can be found under https://doi.org/10.1002/admi.202201189.



**DOI: 10.1002/admi.202201189**

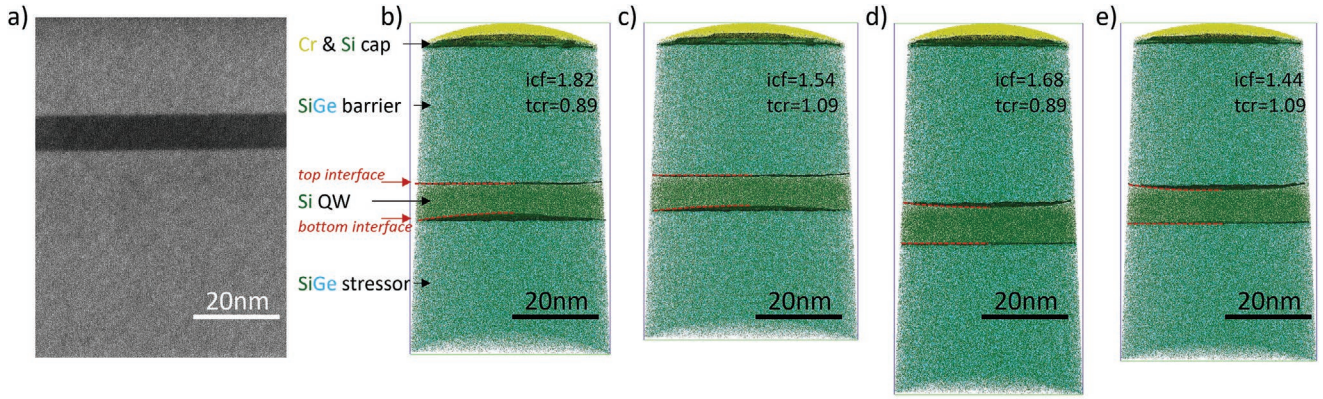


**Figure 1.** a) TEM image and b–e) APT reconstructions of the same SiGe/Si QW structure. All APT reconstructions are from the exact same raw data set. They are reconstructed using different image compression factors (icf) and tip-cap ratios (tcr) as defined in reference [12] and shown in Figure S1 (Supporting Information). Isoconcentration surfaces of 83% Si are highlighted with red dashed lines for convenience. For (b) and (c), the top interface of the QW is flat and the bottom interface is curved, while for (d) and (e), the bottom interface is flat, and the top interface is curved. The TEM image shows that both interfaces of the QW are flat. Note, that the overall dimensions of the reconstructed volumes change even when one interface flat is kept flat.

detector,[12,16] does not allow for a satisfying reconstruction of the interfaces. As shown in Figure 1 and explained in detail in Figure S1 (Supporting Information), moving the projection point (via the image compression factor parameter)[12] or changing the radius of the hemisphere (via the tip-cap ratio parameter)[12] either results in a flat top but curved bottom interfaces (Figure 1b,c) or a flat bottom but curved top interface (Figure 1d,e). This is contradicting TEM measurements (Figure 1a). Furthermore, the width and length of the reconstructed volume (and hence the measured width of, e.g., the QW) can be changed in conjunction with both a flat top (Figure 1b,c) or bottom interface (Figure 1d,e).

The fact that the top and bottom interfaces do not appear simultaneously flat in the same reconstruction using the same reconstruction parameters is not surprising. APT measurements progress by removing single ions from a tip-shaped specimen with a radius of 10–100 nm using field evaporation.[12] The ions are projected onto a single ion detector of several centimeters in diameter, magnifying the two-dimensional surface of the tip by approximately a factor of $10^6$.[12] However, the third dimension, the depth coordinate of each ion is not measured but instead inferred from the arrival sequence. The previously mentioned assumption of the tip possessing a hemispherical cap is however known to be invalid during the analysis of an interface.[17,18]

It has been shown theoretically that the hemispherical constraint imposed by the data reconstruction limits the accuracy of APT,[24–26] particularly near interfaces.[18] In practice, the progression of the hemispherical radius used in the reconstruction is assumed to be directly related to the progression of the tip width via the tcr. The tip width can, for example, be measured by scanning electron microscopy (SEM) as done in this work for the sample shown in Figure 1 and all others shown in the Supporting Information.

Unfortunately, simulations show that the effective radius of the tip's hemisphere changes notably when the analysis progresses through an interface leading to a distortion of the field of view.[18] In particular, the field of view is constricted when going from a material that needs a high(er) electric field to be field-evaporated to a material that needs a low(er) electric field and is widened in the opposite case (low-to-high evaporation field).

We will show that this effect is captured by the protocol introduced here. It is noteworthy that simulations of APT measurements are challenging and time consuming,[13,18,19] that the construction of the input volume for the simulation from the measured APT data is not trivial and that effects relevant for practical APT analyses like the impact of the laser pulse on field evaporation and the formation of complex ions are not yet captured by simulations.[27–29] As a result, it is typically not possible to truly reproduce an APT analysis via a simulation.

As stated above, we postulate that it is possible to obtain an accurate representation of the interface using the standard reconstruction by focusing on getting a correct reconstruction for one interface, and its immediate vicinity, at a time. Effectively, we aim to correctly reconstruct the distorted (either constricted or widened) interface shown in reference [18] in Figure 5 and ignore the effects this has on the rest of the reconstructed data set. As shown in reference [18], the constriction/widening of the field of view around the interface builds up over a length/depth of several 10 nm in simulated data. As epitaxial interfaces are typically only ≈1 nm wide, it is reasonable to expect that the interface itself and its immediate vicinity can be reconstructed with only small aberrations. Indeed, we will be able to show when the image of the interface extracted from such a reconstruction is close to a faithful representation of the real interface and when it is dominated by aberrations induced by the reconstruction. Note that the process presented here can be applied to smooth interfaces of any width; however, we are not aware of simulation results for wider interfaces. As a result, we cannot predict if our postulate that a local optimization results in a faithful representation of the entire interface can hold as the interfaces' width increases beyond a few nanometers.

The process has four steps. First, sets of reconstruction parameters resulting in the steepest possible interfaces are identified. Second, the interfaces in these reconstructions are mapped. Third, the radial symmetry in the interface maps is

evaluated. Fourth, the interface that shows the lowest radial symmetry of all the steepest interfaces is deemed to be the best choice.

## 3. Finding the Steepest Interfaces in the APT Reconstruction Data Space

As indicated in Figure 1, choosing nonoptimal reconstruction parameters leads to an artificial bending of the interface in the reconstructed volume. As a result, in a one-dimensional profile along the axis perpendicular to the interface, the interface will broaden. It is thus straightforward to postulate that, for a typical epitaxial interface that is at most a few nm wide, the optimal reconstruction parameters are the ones that lead to the sharpest interface along the perpendicular axis.

It is shown in **Figure 2** and Figures S2–S4 (Supporting Information) that for the standard reconstruction algorithm used in this work,[12,16] this postulate can be considered a necessary criterion for finding a good interface, but it is not sufficient to select a single best reconstruction of any given interface. When looking at one interface at a time and fixing the tcr, one can always find an icf leading to a steepest interface and vice versa.

The process used to create Figure 2 and Figures S2–S4 (Supporting Information) includes four steps. First, reconstruction parameters are found that align the normal of the interface with the z-axis. Second, the volume is reconstructed for a fixed tcr parameter while varying the icf. The steepness of the interface is evaluated for each reconstruction by fitting a sigmoid function using the approach introduced in reference [30]. This process is repeated for as long as the current interface width is smaller than a given threshold (e.g., less than 150%) of the smallest width found so far. Third, the tcr parameter is changed and the process is repeated until the list of all tcrs is exhausted. Fourth, the process is repeated for the entire list of tcrs on the next interface.

The first step in the process is carried out by reconstructing the APT data set using standard parameters (for a LEAP system: icf = 1.65, tcr = 1, and the radius evolution deducted from a SEM image of the tip) and a zero-degree angle for both tilt angles of the tip.[16] The interface is then constructed using the approach described in the next section. The best fit plane through the interface is calculated and the angles between the normal of the interface and the depth/z-axis are found. These angles are utilized to define the alignment between the tip and the detector in the standard reconstruction protocol[12,16] and ensure that all subsequent reconstructions have the normal of the interface well aligned with the z-axis by default and as a result have a one-dimensional profile along the z-axis that is perpendicular to the interface.

The second step in the process is the brute force step for finding the optimal icf at fixed tcr. As in the first step, a set of initial parameters is chosen, and the APT data are reconstructed based on this choice and the tilt angles extracted in the first step. A one-dimensional profile of the data is calculated by standard methods[12] and a generalized sigmoid/expit function:

$$s(z) = \frac{h}{\left(1 + e^{-\frac{z+z_0}{\tau}}\right)} + b \tag{1}$$

where $h$ is the height of the interface (the concentration difference), $b$ is the base concentration (the concentration on the side with lower $z$ coordinate), $z_0$ is the center position of the interface, and $\tau$ is a measure for the interface width—is fitted to the interface of interest. The interface width is defined as $4\tau$.[30] This is the 12–88 width of the interface, meaning the distance it takes to go from 12% to 88% of the concentration difference ($h$) in $s(z)$. The $4\tau$ interface width is divided by the overall length of the reconstructed volume ($L$) and as such used as a measure for the interface width. The process

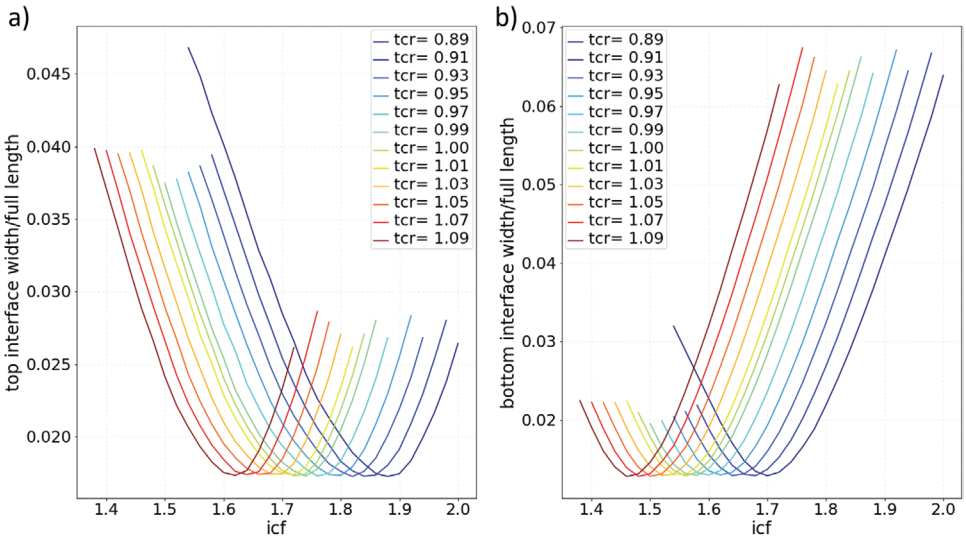


**Figure 2.** a) Top and b) bottom interface width of the QW shown in Figure 1 as a function of tcr and icf. The width of the interfaces is shown relative to the length of the overall volume to account for the different overall length of the various reconstructions (see Figure 1). The icf is changed in steps of 0.02 and to within the error of the method, both interfaces can reach the same width for any given tcr.

is then repeated for the next reconstruction of the same APT data using a different icf until the measure of the interface width in the current reconstruction ($4\tau/L$) is wider than the steepest/thinnest interface found in all previous reconstructions multiplied by some threshold value (the threshold is 1.5 and the icf is changed by +0.02 after every fitting step to generate Figure 2). Once the threshold is reached, the process is repeated by lowering the icf starting from the initial value (in steps if 0.02 in Figure 2) until the threshold is reached a second time. This maps out the curve for one tcr shown in Figure 2. Note, that this process relies on the fact that minimizing the measure of the interface width as a function of the icf is a convex optimization problem and hence the search can be sped up by using, for example, Newton's method or Gradient descent.[31]

In the third step, the entire process in step two is repeated for a list of tcr values, creating all the curves for one interface as shown in Figure 2a.

The fourth and final step is to repeat both steps 2 and 3 for all parallel interfaces of interest in the reconstructed volume creating the data shown in Figure 2a,b.

The process described in this section identifies several potential sets of reconstruction parameters for each interface. The parameters can be selected from the data in Figure 2, for example, by using the steepest/thinnest interface for each tcr. To find the most accurate representation of each interface, the interface is mapped out in the following step and then a second selection criterion is introduced.

## 4. Constructing an Interface from APT Data

Deciding which of the sets of reconstruction parameters selected in the previous step results in the most accurate interface mapping, requires creating a detailed map of the interface. The map is generated in three steps, as illustrated in **Figure 3**.

First, using the reconstructions and the analyses from the previous section, the immediate vicinity of the interface is filtered from the APT data set. For this work, we filter along the z-/depth axis using the interface position and two to three times the ($4\tau$) interface width on both sides to create the interface volume. Figure 3a shows a filtered volume. For illustrative purposes, we chose a cube-shaped volume with a much longer z-extend than usual.

Second, a Voronoi tessellation[32,33] is calculated from the point data within the interface volume as shown in Figure 3b. For all subsequent steps, the Voronoi tessellated data are used. The tessellation can be viewed as a smoothing operation that "spreads out" the detected ions to a finite volume rather than representing them as zero-dimensional points. Effectively, each point associated with an ion is replaced by a three-dimensional polyhedron enclosing the volume that is closer to this particular ion than any other ion in the reconstructed analysis data. Figure 3b shows the Voronoi tessellation of the point set in Figure 3a; the insets in both Figure 3a,b highlight the differences.

Third, a grid is defined in the plane perpendicular to the filter in step one. In this work, this is always the x,y-plane as

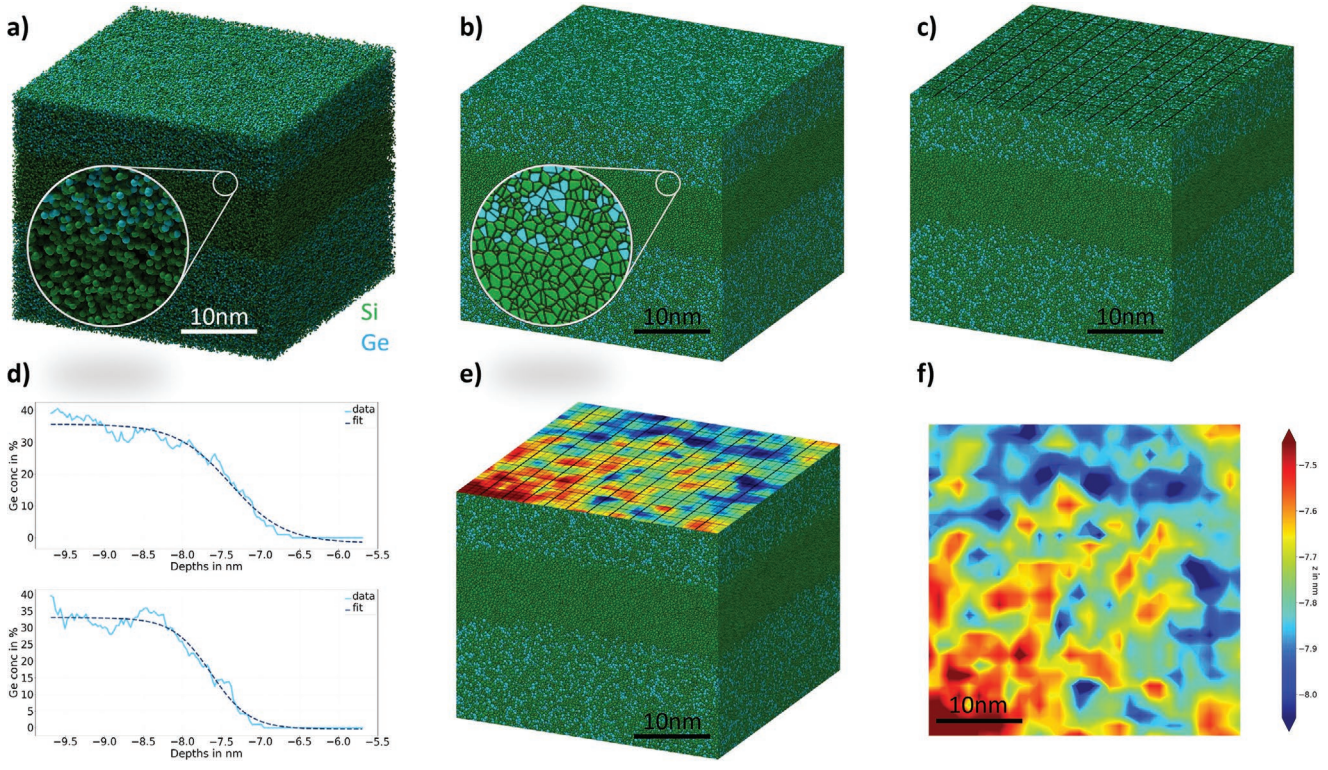


**Figure 3.** a) Interface construction from a set of points (represented as small spheres). b) A Voronoi tessellation is calculated and c) an x,y-grid is dividing the volume in cells of 3 × 3 nm spaced 1 nm apart. d) For each cell, an elemental profile is generated based on the Voronoi tessellation and fitted using a sigmoid function. e,f) The inflection points of the sigmoid functions can then be used to represent the position of the interface at the center-position of each 3 × 3 nm cell.

shown in Figure 3c. For each cell of the grid, a profile along the z-axis is created based on the Voronoi tessellation and fitted using the sigmoid function as discussed above.[30] The set of sigmoid functions is used to represent the interface and calculate the interface positions. We find that we can use cells as small as $3 \times 3$ nm$^2$ in the x,y-plane and still have all fits reliably converge to the resulting profiles using the Levenberg–Marquardt algorithm.[34,35] The data set shown in Figure 3 is split into $3 \times 3$ nm$^2$ cells spaced 1 nm apart and thus partially overlapping to create the map shown in Figure 3e,f. This results in $36 \times 36$ profiles and hence 1296 fit functions for the Germanium profiles that represent the interface. Figure 3d exemplary shows two of the profiles and the respective sigmoid fits. The maps in Figure 3e,f are generated by mapping the inflection point of the sigmoid function for each cell.

Note, that profiles in the Voronoi tessellation are generated by creating cuts along the z-axis every 0.03 nm and use all ions whose associated polyhedron is in contact with the cut plane to calculate the concentration at the particular z-coordinate (i.e., depth).

## 5. Finding the Interface with the Lowest Reconstruction Aberrations

In order to find the interface that is the least distorted by the standard APT reconstruction utilized here, we make use of the cylindrical symmetry that the standard reconstruction imposes on the measured data.[16] As a result, aberrations introduced by the reconstruction in a plane perpendicular to the z-axis, like the interfaces mapped in the previous section, show circular symmetry. Note, that there is no reason for the underlying material to show any symmetric features with respect to the position that was arbitrarily chosen to be the middle of the reconstructed data set during the tip preparation and the APT measurement process. Furthermore, it is important to realize that the focus on circular symmetries limits the application of this part of our process to interfaces imaged such that their normal axis is closely aligned with the tip axis. For interfaces with a different alignment, other symmetries would be expected.

We use the Fourier–Bessel transform, also known as the zero-order Hankel transform,[36] to decompose the interface maps into spherical waves around the middle of the reconstruction. The interface map with the lowest spectral density between 0 and 1nm$^{-1}$ in this decomposition is the interface with the lowest spectral power density in radial waves with wavelength of more than 1 nm in real space. We postulate that this interface is the least affected by reconstruction artifacts and hence the optimal interface to use to characterize the underlying material, the sharpest interface with the least distortions introduced by the reconstruction.

**Figure 4** exhibits the evaluation of interfaces for the data set shown in Figures 1 and 2. Additional results are outlined in Figures S5–S8 (Supporting Information). Note, that in agreement with simulations,[18] the reconstructed top interface has a wider field of view (67 nm) than the reconstructed bottom interface (64 nm).

Each of the 12 interfaces, selected as the steepest from each of the 12 convex tcr curves in Figure 2, is mapped four times using the algorithm described in the previous section with different cell sizes and step width. For each of the four selected sets of mapping parameters, the interfaces are ranked from the lowest spectral density (best interface) to the highest spectral density (worst interface). Figure 4a,d shows the ranking results for the top (4a) and bottom (4d) interface of the QW.

While the ranking is not the same for each choice of parameters, there are clearly interface maps that consistently rank high and others that consistently rank low for the maps of both top and bottom interface. This is in-spite of the fact that even the maps for the best (Figure 4e) and worst bottom interfaces (Figure 4f) look alike to the eye. The average RMS roughness for all 12 of the sharpest top and bottom interfaces at a fixed tcr and the respective standard deviations evaluated using cells of $3 \times 3$ nm$^2$ and a 1 nm step, a cell of $3 \times 3$ nm$^2$ and a 2 nm step, a cell of $4 \times 4$ nm$^2$ and 1 nm step, a cell of $4 \times 4$ nm$^2$ and 2 nm step in the interface mapping procedure is shown in Table 1, row 1.

The standard deviation between different interfaces characterized with the same parameters is 10 pm or less and the observed change between difference choices for the cell size and step results is also on the order of a few 10 pm.

The data in Figure 4e,f clearly show that the map of the bottom interface is dominated by radial features and hence by aberrations caused by reconstruction artifacts. For the interface maps of the top interface shown in Figure 4b,c, radial features are not dominant but rather localized near the edge of the field of view. We can think of two reasons to explain the discrepancy.

First, the top interface is imaged when going from a low evaporation field to a high-evaporation field material (see Figure 5b in reference [18]), while the opposite is true for the bottom interface (see Figure 5a in reference [18]). It is possible that artifacts are more pronounced in the second case. Second, the QW is only 6–7 nm wide and the top layer is hence still present on the apex of the tip when the bottom interface enters the field of view. The simulations shown in reference [18] indicate that the field of view during the measurement changes for a few 10 nm around the interfaces. This means that it takes a few 10 nm of material evaporation for the tip analyzed in APT to find a steady shape after passing through an interface. It is hence likely that the tip does not revert to its steady shape before passing the bottom interface causing additional distortions.

High-angle annular dark-field scanning-TEM (HAADF-STEM) images of the QW show an interface width of ≈0.7 nm for the top and 0.8 nm for the bottom interface. The APT reconstructions shown in Figure 4b,e have an interface width of 1.3 nm for the top and 1.1 nm for the bottom interface. We expect the STEM images to be reliable both in terms of the relative widths of the interfaces and the absolute interface width on the scale of the TEM lamella thickness (≈50 nm).[30]

Two issues are hence apparent: first, the interfaces appear wider in APT than in HAADF-STEM and second, the top interface appears wider than the bottom interface, which is the opposite of the HAADF-STEM result. We address these two issues in the following.

Artificially limiting the field-of-view (FoV) and a density correction along the z-axis can both alleviate the radial features visible on the bottom interface and create a qualitative agreement with HAADF-STEM, as shown in reference [30]. As the

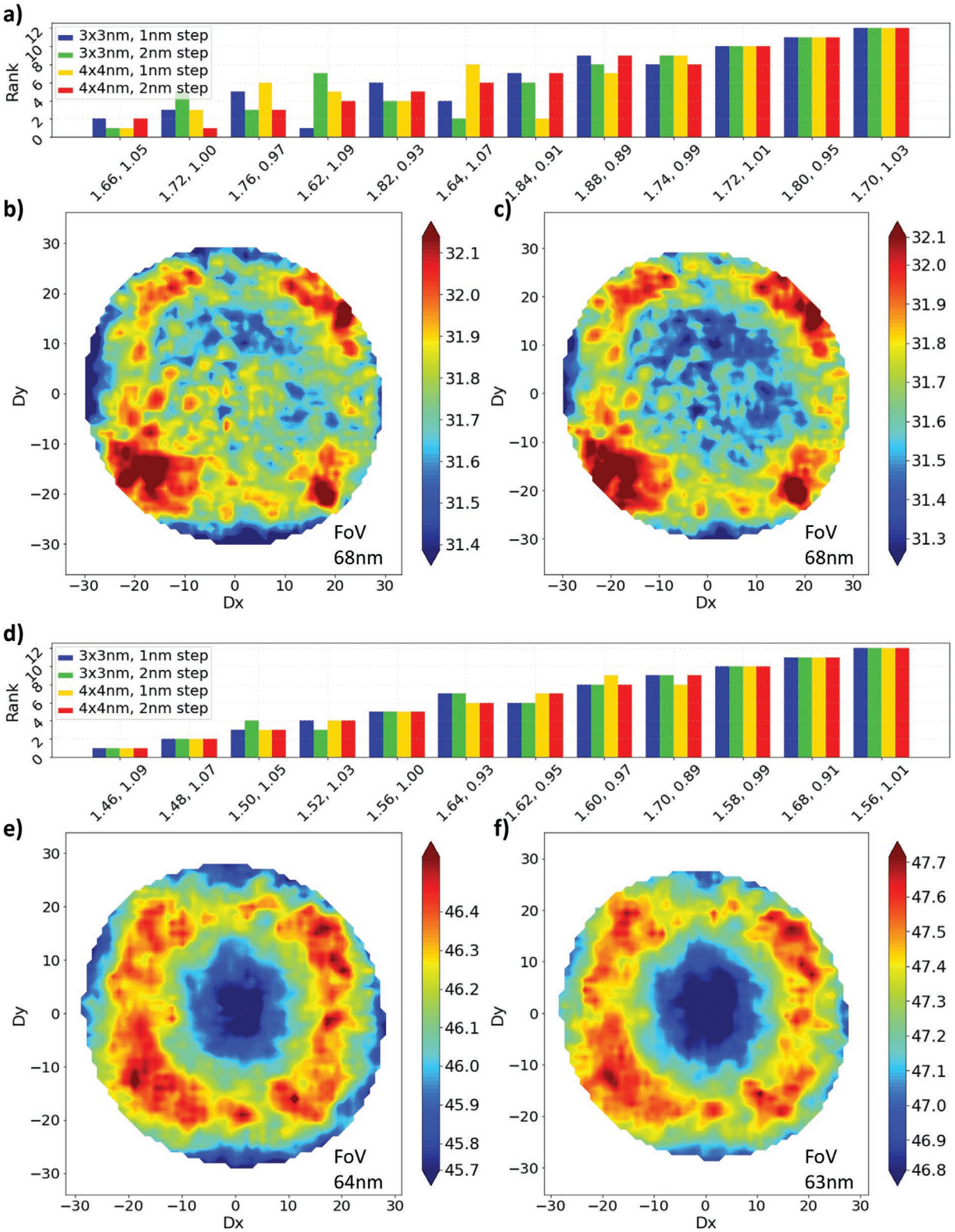


**Figure 4.** Evaluation of: a–c) the top and e,f) bottom interface maps of the data set in Figures 1 and 2. a,d) The ranking shows the best of the 12 interfaces selected from Figure 2 on the left and the worst on the right. Each interface is mapped four times with a different cell sizes and step width and four rankings are generated using the power spectral density of the Fourier–Bessel transform. The reproducibility of the ranking is shown in (a) and (d). The best interface is the one with the smallest average rank and its map is shown in (b, top) and (e, bottom). The worst interface is the one with the largest average rank and its map is shown in (c, top) and (f, bottom). For each interface, the implied field of view is indicated. The differences in field of view between top and bottom interface agree with expectations from simulations.[18]

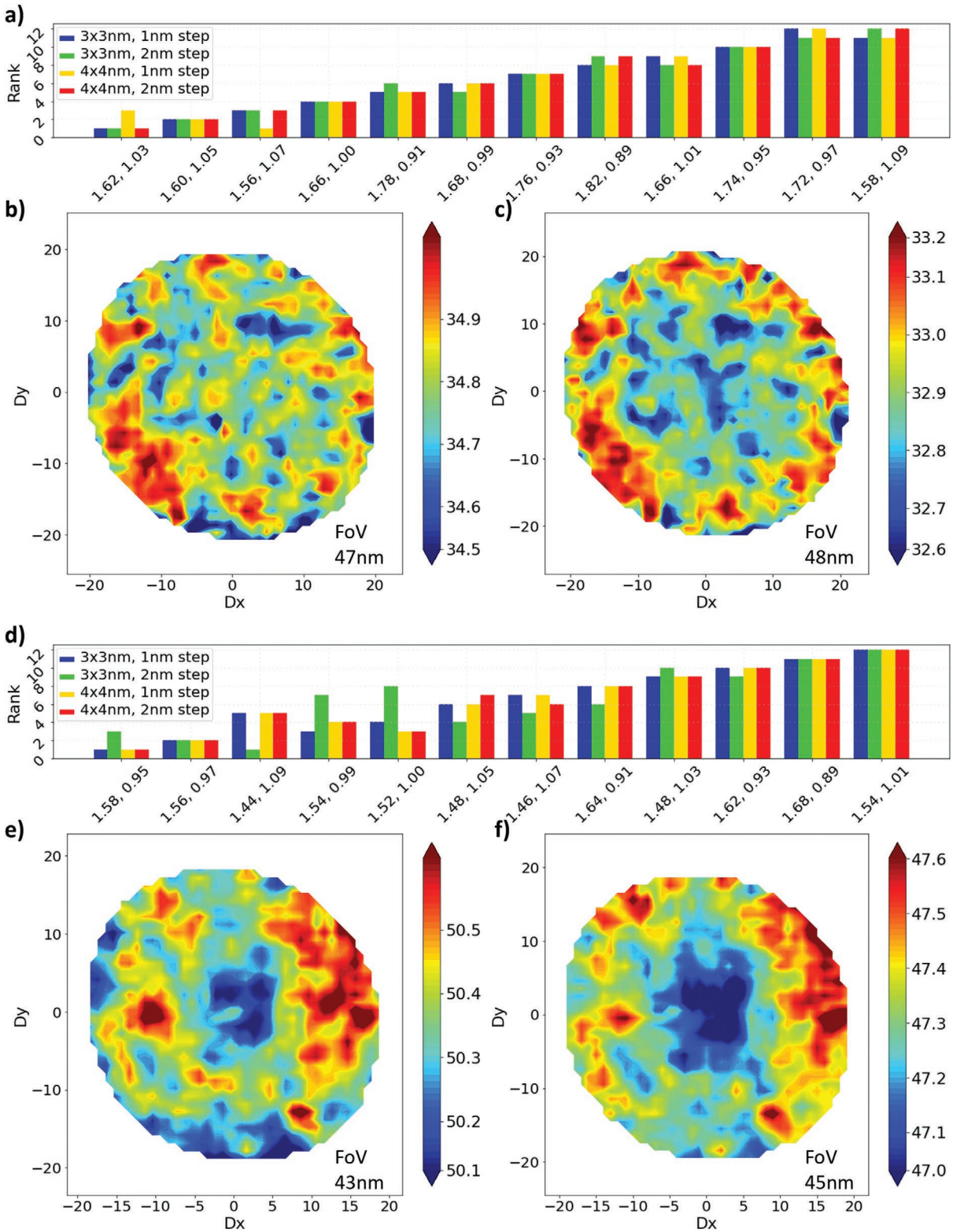


**Figure 5.** Evaluation of: a–c) the top and e,f) bottom interface maps of the data set in Figures 1 and 2 when using only the inner 4 cm of the detector and rescaling the depth axis based on density.[30] a,d) The ranking shows the best of the 12 interfaces selected from Figure 2 on the left and the worst on the right. Each interface is mapped four times with a different cell sizes and step width and four rankings are generated using the power spectral density of the Fourier–Bessel transform. The reproducibility of the ranking is shown in (a) and (d). The best/worst interface is the one with the smallest/largest average rank and its map is shown in (b/c, top) and (e/f, bottom). For each interface, the implied field of view is indicated. The differences between top and bottom interface agree with expectations from simulations.[18]

**Table 1.** Results for the RMS roughness and interface width found for the different sets of samples discussed in the manuscript showing both the in-between reconstructions of the same sample variations (rows 1, 3, 5) and the in-between APT analyses on the same sample variations (rows 2, 4, 6). The roughness is calculated for all four parameter sets used for the interface construction shown in Figures 4 and 5 and Figures S4–S17 (Supporting Information).

| Evaluation | | RMS roughness | | Interface width | |
|---|---|---|---|---|---|
| | | Top | Bottom | Top | Bottom |
| 6 cm detector: 12 steepest interfaces of optimization step in Figure 2 (*in-between APT reconstruction variations*) | 3 × 3, 1 | 0.151 ± 0.004 nm | 0.171 ± 0.007 nm | 1.30 ± 0.04 nm | 1.10 ± 0.03 nm |
| | 3 × 3, 2 | 0.150 ± 0.010 nm | 0.169 ± 0.008 nm | | |
| | 4 × 4, 1 | 0.130 ± 0.005 nm | 0.162 ± 0.008 nm | | |
| | 4 × 4, 2 | 0.131 ± 0.005 nm | 0.161 ± 0.008 nm | | |
| 6 cm detector: Five interfaces of Figure 4 and Figures S4–S7 (Supporting Information) (*in-between measurement variation*) | 3 × 3, 1 | 0.151 ± 0.012 nm | 0.154 ± 0.009 nm | 1.29 ± 0.08 nm | 1.08 ± 0.02 nm |
| | 3 × 3, 2 | 0.151 ± 0.011 nm | 0.154 ± 0.009 nm | | |
| | 4 × 4, 1 | 0.130 ± 0.011 nm | 0.131 ± 0.007 nm | | |
| | 4 × 4, 2 | 0.130 ± 0.010 nm | 0.132 ± 0.009 nm | | |
| 4 cm detector: 12 steepest interfaces of optimization step in Figure S2 (Supporting Information) (*in-between APT reconstruction variations*) | 3 × 3, 1 | 0.089 ± 0.007 nm | 0.087 ± 0.003 nm | 1.01 ± 0.03 nm | 0.71 ± 0.02 nm |
| | 3 × 3, 2 | 0.086 ± 0.008 nm | 0.087 ± 0.003 nm | | |
| | 4 × 4, 1 | 0.069 ± 0.007 nm | 0.070 ± 0.002 nm | | |
| | 4 × 4, 2 | 0.068 ± 0.008 nm | 0.068 ± 0.003 nm | | |
| 4 cm detector: Five interfaces of Figures S8–S11 (Supporting Information) (*in-between measurement variation*) | 3 × 3, 1 | 0.081 ± 0.003 nm | 0.086 ± 0.008 nm | 1.00 ± 0.06 nm | 0.71 ± 0.03 nm |
| | 3 × 3, 2 | 0.081 ± 0.002 nm | 0.085 ± 0.007 nm | | |
| | 4 × 4, 1 | 0.061 ± 0.001 nm | 0.068 ± 0.009 nm | | |
| | 4 × 4, 2 | 0.060 ± 0.003 nm | 0.067 ± 0.008 nm | | |
| 4 cm detector, density corrected: 12 steepest interfaces of Figure S3 (Supporting Information) (*in-between APT reconstruction variations*) | 3 × 3, 1 | 0.100 ± 0.003 nm | 0.097 ± 0.006 nm | 0.70 ± 0.03 nm | 1.02 ± 0.04 nm |
| | 3 × 3, 2 | 0.096 ± 0.005 nm | 0.097 ± 0.006 nm | | |
| | 4 × 4, 1 | 0.072 ± 0.005 nm | 0.084 ± 0.006 nm | | |
| | 4 × 4, 2 | 0.071 ± 0.005 nm | 0.081 ± 0.007 nm | | |
| 4 cm detector, density corrected: Five interfaces of Figures S12–S16 (Supporting Information) (*in-between measurement variation*) | 3 × 3, 1 | 0.096 ± 0.018 nm | 0.088 ± 0.010 nm | 0.67 ± 0.03 nm | 1.03 ± 0.03 nm |
| | 3 × 3, 2 | 0.081 ± 0.009 nm | 0.086 ± 0.011 nm | | |
| | 4 × 4, 1 | 0.059 ± 0.006 nm | 0.064 ± 0.008 nm | | |
| | 4 × 4, 2 | 0.061 ± 0.005 nm | 0.063 ± 0.006 nm | | |

interface fitting and construction method introduced above is derived from the method introduced in reference [30], we can use the same method to rescale the depth-/z-axis and correct for the density variations to first order on a limited field of view and redo the entire analysis.

The effect on the interface mapping created by limiting the FoV using a virtual detector size to 4 cm is shown in Figures S3, S9–S13 (Supporting Information). The effect of the density correction on this limited FoV data set is shown in **Figure 5** and Figures S4, S14–S17 (Supporting Information). All measures for the interface width and the roughness resulting from these analyses are summarized in **Table 1**.

Figure S18 (Supporting Information) shows the measured interface width as a function of the detector size. In agreement with the previous work,[30] a reduction of the FoV to about half the detector radius results in matching interface widths between APT and HAADF-STEM. This shows that up to 75% of the data set acquired in APT cannot be reconstructed with sufficient accuracy to characterize buried interfaces on an Ångstrom scale due to the limitations of the standard reconstruction algorithm even when resorting to a local reconstruction of the volumes near the interfaces.

Table 1 highlights the reproducibility of the method. With the measured, the interface width having errors of significantly less than 0.1 nm and the measured RMS roughness having errors of around 0.01 nm or less both when comparing the result of different measurement and different reconstructions.

## 6. Conclusions

We have introduced a new, fully automated process to characterize buried interfaces in a highly reproducible manner by systematically reducing APT-related artifacts. It is based on the idea that aberrations caused by the algorithm used to construct the tomography volume[12,13,16,26] can be overcome or at least decreased by focusing on creating a tomography of only the interface and its immediate vicinity using a brute force approach and two rating criteria to select the best image of the interface.

The process progresses in four steps. First, the normal of the interface is aligned with the z-/depth axis of the reconstructed volume. Second, brute force is used to find the set of reconstruction parameters that result in the steepest possible interfaces,

the first criterion. Third, the interfaces in these reconstructions are mapped using a Voronoi tessellation of the acquired point data. Fourth, the radial symmetry in the interface maps is evaluated. The interface that shows the lowest radial symmetry of all the steepest interfaces is deemed to be the best choice, the second criterion.

As shown in Table 1, the process results in highly reproducible characteristics for the roughness—showing errors on the orders of 10 pm both within and between samples—and the width of each interface—showing errors on the sub Ångstrom scale—even when the interface maps are dominated by aberrations related to the data reconstruction. Note, that this implies, that the aberrations are systematic errors that can potentially be corrected by a more advanced reconstruction algorithm. By artificially limiting the field of view of the measurement, we can sort out the aberrations and find consistent results when comparing APT and HAADF-STEM imaging, in agreement with the previous work.[30]

The framework introduced here is flexible and can readily be applied to APT data sets that image a suitably aligned interface. The sigmoid function used to fit the interface can be replaced with other step functions. Furthermore, delta layers[37] or multiquantum wells[38] can be analyzed using double or multisigmoid functions or other multistep functions, respectively. The power spectral density of the Fourier–Bessel transformation employed here to evaluate the symmetries of each interface map is only one of a number of potential evaluations that can be done to find the "best" of the interfaces selected from Figure 2. Reisfeld's generalized symmetry transform[39] and the fast radial symmetry transform[40] are two other potential candidates allowing for a similar evaluation that can be used to supplement or support the evaluation criterion chosen here. The generalized symmetry transform in particular may allow to evaluate interfaces that are not perpendicular to the z-/depth axis by enabling the search for nonradial symmetries.[39] Furthermore, the local reconstruction/brute force/rating approach for interfaces can readily be applied to new data reconstruction algorithms currently in development.[18–20,24]

## 7. Experimental Section

*Atom Probe Tomography*: Samples for APT were prepared in a FEI Helios Nanolab 660 dual-beam scanning electron microscope using a gallium-focused ion beam at 30, 16, and 5 kV. A 150–200 nm thick chromium capping layer was deposited on the sample via thermal evaporation before FIB irradiation to minimize the implantation of gallium ions into the region of interest. APT was carried out in a LEAP 5000XS tool from Cameca. The system utilizes a picosecond laser to generate pulses at a wavelength of 355 nm. For the analysis, all samples were cooled to a temperature of 25 K. The experimental data were collected at a laser pulse rate of 200–500 kHz at a laser power of 8–10 pJ.

*Data Treatment*: For the Voronoi tessellation, the reconstructed data sets were exported to Python 3.9.2 and then tessellated using the scipy.spatial.Voronoi class of SciPy 1.6.2. Profiles were fitted using the scipy.optimize.curve_fit class of SciPy 1.6.2.

*Si/SiGe Heterostructure Growth*: The Si/SiGe heterostructures were grown on a 100-mm *n*-type Si(001) substrate using an Epsilon 2000 (ASMI)-reduced pressure chemical vapor deposition reactor equipped with a Silane gas cylinder (1% dilution in $H_2$). The $Si_{0.7}Ge_{0.3}$ strain-relaxed buffer below the quantum well was grown at a temperature of 625 °C, followed by growth interruption and quantum well growth at 750 °C.

## Supporting Information

Supporting Information is available from the Wiley Online Library or from the author.

## Acknowledgements

O.M. acknowledges support from the NSERC Canada (Discovery, SPG, and CRD Grants), Canada Research Chairs, Canada Foundation for Innovation, Mitacs, PRIMA Québec, and Defence Canada (Innovation for Defence Excellence and Security, IDEaS). This work was supported in part by the Army Research Office (grant No. W911NF-17-1-0274). The views and conclusions contained in this document are those of the authors and should not be interpreted as representing the official policies, either expressed or implied, of the Army Research Office (ARO), or the U.S. Government. The U.S. Government is authorized to reproduce and distribute reprints for Government purposes notwithstanding any copyright notation herein.

## Conflict of Interest

The authors declare no conflict of interest.

## Data Availability Statement

The data that support the findings of this study are available from the corresponding author upon reasonable request.

## Keywords

atom probe tomography, atomic scale microscopy, epitaxial interfaces, semiconductor heterostructures

Received: May 28, 2022
Revised: October 27, 2022
Published online:

[1] D. Paul, *Laser Photonics Rev.* **2010**, *4*, 610.
[2] C. T. Carver, J. J. Plombon, P. E. Romero, S. Suri, T. A. Tronic, R. B. Turkot, Jr., *ECS J. Solid State Sci. Technol.* **2015**, *4*, N5005.
[3] Y. Zhang, X. Ai, X. Yin, H. Zhu, H. Yang, G. L. Wang, J. J. Li, A. Du, C. Li, W. Huang, L. Xie, *IEEE Trans. Electron. Device* **2021**, *68*, 2604.
[4] G. Scappucci, C. Kloeffel, F. A. Zwanenburg, D. Loss, M. Myronov, J.-J. Zhang, S. D. Franceschi, G. Katsaros, M. Veldhorst, *Nat. Rev. Mater.* **2021**, *6*, 926.
[5] B. P. Wuetz, M. P. Losert, A. Tosato, M. Lodari, P. L. Bavdaz, L. Stehouwer, P. Amin, J. S. Clarke, S. N. Coppersmith, A. Sammak, M. Veldhorst, M. Friesen, G. Scappucci, *Phys. Rev. Lett.* **2010**, *125*, 186801.
[6] H. Kroemer, *Rev. Mod. Phys.* **2001**, *73*, 783.
[7] Editorial, *Nat. Mater.* **2012**, *11*, 91.
[8] F. J. Giessibl, *Science* **1995**, *267*, 68.
[9] T. J. Z. Stock, O. Warschkow, P. C. Constantinou, J. Li, S. Fearn, E. Crane, E. V. S. Hofmann, A. Kölker, D. R. McKenzie, S. R. Schofield, N. J. Curson, *ACS Nano* **2020**, *14*, 3316.
[10] C. Ophus, *Mirosc. Microanal.* **2019**, *25*, 563.
[11] S. Reboh, R. Coquand, N. Loubet, N. Bernier, E. Augendre, R. Chao, J. Li, J. Zhang, R. Muthinti, V. Boureau, T. Yamashita, in *2019 IEEE*

*International Electron Devices Meeting (IEDM)*, IEEE, San Francisco, USA **2019**.
[12] D. J. Larson, T. J. Prosa, R. M. Ulfig, B. P. Geiser, T. F. Kelly, *Local Electrode Atom Probe Tomography*, Springer, New York, NY, USA **2013**.
[13] J. Barnes, A. Grenier, I. Mouton, S. Barraud, G. Audoit, J. Bogdanowicz, C. Fleischmann, D. Melkonyan, W. Vandervorst, S. Duguay, N. Rolland, *Scr. Mater.* **2018**, *148*, 91.
[14] D. Blavette, E. Cadel, A. Fraczkiewicz, A. Menand, *Science* **1999**, *286*, 2317.
[15] S. Koelling, O. Richard, H. Bender, M. Uematsu, A. Schulze, G. Zschaetzsch, M. Gilbert, W. Vandervorst, *Nano Lett.* **2013**, *13*, 2458.
[16] P. Bas, A. Bostel, B. Deconihout, D. Blavette, *Appl. Surf. Sci.* **1995**, *87–88*, 298.
[17] S. Koelling, M. Gilbert, J. Goossens, A. Hikavyy, O. Richard, W. Vandervorst, *Appl. Phys. Lett.* **2009**, *95*, 144106.
[18] N. Rolland, F. Vurpillot, S. Duguay, B. Mazumder, J. Speck, D. Blavette, *Microsc. Microanal.* **2017**, *23*, 247.
[19] D. Beinke, C. Oberdorfer, G. Schmitz, *Ultramicroscopy* **2016**, *165*, 34.
[20] C. Fletcher, M. P. Moody, D. Haley, *J. Phys. D: Appl. Phys.* **2020**, *53*, 475303.
[21] W. I. L. Lawrie, H. G. J. Eenink, N. W. Hendrickx, J. M. Boter, L. Petit, S. V. Amitonov, M. Lodari, B. P. Wuetz, C. Volk, S. G. J. Philips, G. Droulers, N. Kalhor, F. v. Riggelen, D. Brousse, A. Sammak, L. M. K. Vandersypen, G. Scappucci, M. Veldhorst, *Appl. Phys. Lett.* **2020**, *116*, 080501.
[22] B. Paquelet Wuetz, M. P. Losert, S. Koelling, L. E. A. Stehouwer, A.-M. J. Zwerver, S. G. J. Philips, M. T. Mądzik, X. Xue, G. Zheng, M. Lodari, S. V. Amitonov, N. Samkharadze, A. Sammak, L. M. Vandersypen, R. Rahman, S. N. Coppersmith, O. Moutanabbir, G. Scapucci, (Preprint) arXiv, 2112.09606, unpublished, December **2021**.
[23] J. P. Snyder, *Map Projections A Working Manual*, U.S. Geological Survey, Washington DC **1987**.
[24] F. Vurpillot, M. Gruber, G. Da Costa, I. Martin, L. Renaud, A. Bostel, *Ultramicroscopy* **2011**, *111*, 1286.
[25] D. Larson, B. Gault, B. Geiser, F. De Geuser, F. Vurpillot, *Curr. Opin. Solid State Mater. Sci.* **2013**, *17*, 236.
[26] S. Koelling, N. Innocenti, A. Schulze, M. Gilbert, A. Kambham, W. Vandervorst, *J. Appl. Phys.* **2011**, *109*, 104909.
[27] J. Houard, A. Vella, F. Vurpillot, B. Deconihout, *Phys. Rev. B* **2010**, *81*, 125411.
[28] J. Houard, A. Vella, F. Vurpillot, B. Deconihout, *Phys. Rev. B* **2010**, *84*, 033405.
[29] M. Karahka, H. Kreutzer, *Ultramicroscopy* **2015**, *159*, 156.
[30] O. Dyck, D. Leonard, L. Edge, C. Jackson, E. Pritchett, P. Deelman, J. Poplawsky, *Adv. Mater. Interfaces* **2017**, *4*, 1700622.
[31] S. Boyd, V. L. , *Convex Optimization*, Cambridge University Press, Cambridge, UK **2004**.
[32] G. Voronoi, *Journal für die reine und angewandte Mathematik* **1908**, *133*, 97.
[33] G. Voronoi, *Journal für die reine und angewandte Mathematik* **1908**, *134*, 198.
[34] K. Levenberg, *Quart. Appl. Math* **1944**, *2*, 164.
[35] D. W. Marquardt, *SIAM J. Appl. Math.* **1963**, *11*, 431.
[36] W. G. Faris, *Radial Functions and the Fourier Transform, Notes for Math 583A*, University of Arizona, USA **2008**.
[37] H.-J. Gossman, E. F. Schubert, *Crit. Rev. Solid State Mater. Sci.* **1993**, *18*, 1.
[38] I. A. Fischer, C. Clausen, D. Schwarz, P. Zaumseil, G. Capellini, M. Virgilio, M. C. da Silva Figueira, S. Birner, S. Koelling, P. Koenraad, M. R. S. Huang, C. Koch, T. Wendav, K. Busch, J. SChulze, *Phys. Rev. Mater.* **2020**, *4*, 024601.
[39] D. Reisfeld, H. Wolfson, Y. Yeshurun, *Int. J. Comput. Vis.* **1995**, *14*, 119.
[40] G. Loy, A. Zelinsky, *IEEE Trans. Pattern Anal. Mach. Intell.* **2003**, *25*, 959.